Scattering from frequency selective surfaces: An efficient set of V-dipole basis functions

Poulsen, Sören

2000

CODEN:LUTEDX/(TEAT-7083)/1-20/(2000)

Revision No. 1: February 2002

Scattering from frequency selective surfaces: An efficient set of V-dipole basis functions

Sören Poulsen

Department of Electroscience
Electromagnetic Theory
Lund Institute of Technology
Sweden

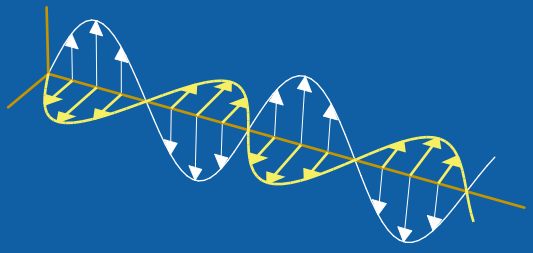

Sören Poulsen
Email: Soren.Poulsen@acab.se

Applied Composites AB
P.O. Box 163
SE-341 23 Ljungby
Sweden

and

Department of Electroscience
Electromagnetic Theory
Lund Institute of Technology
P.O. Box 118
SE-221 00 Lund
Sweden

Editor: Gerhard Kristensson

Abstract

In this paper a novel set of V-dipole basis functions is introduced. These basis functions are used to approximate the induced surface current density on an infinite, plane frequency selective surface (FSS). The elements of the FSS are supposed to consist of straight sections and bends. Two groups of elements which the present V-dipole basis functions can be applied to are identified, namely the center connected elements and the loop type elements. Using the established spectral Galerkin method, where the method of moment (MoM) procedure is carried out in the spectral domain, we determine the reflection and transmission coefficients of the FSS. The convergence of the solution is demonstrated both for existing bases and the present V-dipole basis functions. It is found that the double infinite Floquet sum diverges when existing, discontinuous, basis functions are used, but that convergence is obtained for the present basis functions. Therefore, care needs to be exercised and it would seem discontinuous bases should be avoided.

1 Introduction

In this paper, we use an established method, sometimes referred to as the *spectral Galerkin method* [24], to calculate the reflection and transmission coefficients of an infinite, plane frequency selective surface (FSS). In the spectral Galerkin method, the formulation is carried out in the spectral domain, where the convolution in the integral equation is reduced to an algebraic relation. The incident plane wave induces an electric surface current at the conducting parts of the FSS (magnetic currents are used for slot FSSs). To determine this current density, it is expanded in entire domain basis functions, with unknown current coefficients. The current coefficients are then determined from a linear system of equations, obtained by imposing the boundary condition at the conducting surface. Once the surface current density is known, the scattered fields are easily obtained. More details on the spectral Galerkin method are found elsewhere [20, 24, 28].

In practical FSS applications, such as low observable radomes, two or more layered FSSs are often needed to obtain required bandwidth *etc.* Moreover, due to mechanical requirements, and for scan independence, the FSSs are often embedded in a dielectric media. Multilayered FSSs are analyzed by either the scattering matrix method [4, 5, 7, 22] or a full-wave moment method [28]. The full-wave moment method determines the current distribution on each FSS screen simultaneously. If N_1, N_2, ..., N_n are the number of unknowns on screen 1, screen 2, ..., and screen n, respectively, then the full-wave moment method solution involves a matrix with $(N_1 + N_2 + \ldots + N_n)^2$ elements. Thus, to get acceptable computer run time, it is extremely important that only a few number of unknowns on each FSS screen are required to get adequate results. Hence, it is reasonably to require that a few number of basis functions approximate the induced surface current density well, even for complex element geometries.

The concept of relative convergence was introduced by Mittra [13] for the particular case of the mode-matching formulation of a bifurcated waveguide junction

problem. Mittra found that unless the correct ratio of the number of modes is taken in the two regions, a correct solution cannot be obtained as the number of modes approaches infinity [13]. Convergence aspects of the FSS solutions have many similarities, and the concept of relative convergence has been used for the FSS analysis as well [10, 23]. However, Webb, Grounds and Mittra [26] found no evidence for the existence of a relative convergence phenomenon for the FSS analysis in general. Instead, they showed that one should rely on absolute convergence, where a sufficiently large number of satisfactory basis functions are used together with a large number (approaching infinity) included Floquet modes [26].

Webb, Grounds and Mittra [26] found that the Floquet sum corresponding to the pulse function is divergent. Later, it was found that the basis functions should fulfill a continuity condition [19], otherwise the double infinite sum of Floquet modes corresponding to a discontinuous basis function is divergent. Since the Floquet sum is divergent, the result is strongly dependent of how many Floquet modes that are included. Therefore, care needs to be exercised and it would seem discontinuous bases should be avoided.

The main objective of the present V-dipole basis functions is that absolute convergence is obtained, since the Floquet sums are convergent. We simply include Floquet modes until the Floquet sum has converged numerically. To sum up, the V-dipole basis functions are introduced for two reasons:

Efficiency: Only a few number of basis functions are required to obtain adequate solutions.

Convergence: They yield convergent Floquet sums, in contrast to discontinuous bases.

In the next section, we define the V-dipole basis functions, and provide tools for the assembly of the FSS element. The element, which consists of straight sections and bends, is easily assembled by moving and rotating generic basis functions, called the straight section and circular current basis functions, respectively. We demonstrate the efficiency of the V-dipole basis functions by considering two FSS arrays, *i.e.*, the tripole and the hexagonal loop array. Regarding the tripole array, calculated transmission and reflection coefficients are compared with measured ones, and excellent agreement is found. When it comes to the hexagonal loop element, we compare predicted reflection with results obtained by the PMM program [15–17]. PMM, the periodic method of moment program, is developed at the *ElectroScience Laboratory*, Ohio State University.

Finally, we demonstrate the convergence of the solution when existing and the present basis functions are used.

2 Methods

2.1 The generic basis functions

The element, whether it is a center connected or a loop type element, is divided into straight sections and bends. In this section we define the generic basis functions that are applied to the straight sections and the bends of the element. The approach is to let the amplitude vary at the straight sections, while it is constant at the bends. Therefore, we introduce the length L, which for center connected elements equals the length of the V-dipole, that is, $L/2$ is the length of the arms. On the other hand, for loop type elements, L is the total length of the loop. Moreover, we let x_s and x_e define the start and the end points, respectively, of the straight section. Thus, by making an appropriate choice of x_s and x_e, the straight section starts and ends at specific amplitudes.

To this end, the straight section functions are defined as

$$j_p^+(x; x_s, x_e) := \sin p\pi x/L, \quad p = 1, 2, \dots$$

and

$$j_p^\circ(x; x_s, x_e) := \begin{cases} \cos p\pi x/L & p = 0, 2, 4, \dots \\ \sin(p+1)\pi x/L & p = 1, 3, \dots \end{cases}$$

where $x_s \le x \le x_e$. Outside the interval $x_s \le x \le x_e$ the straight section functions vanish. The functions j_p^+ are applied to center connected elements, and they are zero at $x = 0$ and $x = L$ (which turns out to be the endpoints of the strip considered). On the other hand, the functions j_p° are applied to loop elements. Since the start and end point are equal for loops, $j_p^\circ(x; 0, L)$ do not necessarily vanish at $x = 0$ and $x = L$. However, $j_p^\circ(0; 0, L) = j_p^\circ(L; 0, L)$. Notice that $\{j_p^\circ(x; 0, L)\}_{p=0}^\infty$ is a complete set on $0 \le x \le L$.

We introduce the generic straight section basis functions as

$$\boldsymbol{j}_p^{+,\circ}(\boldsymbol{\rho}; x_s, x_e) := \hat{x} j_p^{+,\circ}(x; x_s, x_e), \quad \boldsymbol{\rho} \in S_s \tag{2.1}$$

where $S_s := \{\boldsymbol{\rho} : x_s \le x \le x_e,\ -W \le y \le 0\}$. Outside the region S_s, $\boldsymbol{j}_p^{+,\circ}(\boldsymbol{\rho}; x_s, x_e)$ vanishes. Throughout this paper, $\boldsymbol{\rho} := \hat{x}x + \hat{y}y$ is a point (or vector) in the xy-plane (the plane of the FSS). We assume that the width of the straight section is small so that it is a good approximation to assume that the current is directed along the straight section only. Moreover, the current is approximated to be constant over the width, that is, we do not take the edge condition, which says that the current component parallel to an edge is singular, into account.

At the bends we apply the circular current basis function defined by

$$\boldsymbol{j}^c(\boldsymbol{\rho}; v) := (-\hat{x}y + \hat{y}x)(x^2 + y^2)^{-1/2}, \quad \boldsymbol{\rho} \in S_c \tag{2.2}$$

where $S_c := \{\boldsymbol{\rho} \in \mathbb{R}^2 : 0 < \rho < W, 0 < \arccos x/\rho < v,\ y > 0\}$, where $\rho := |\boldsymbol{\rho}|$. Here, v is the angle of the bend. The support of the generic straight section basis functions and the circular current basis function is shown in Figure 1, where also the current lines of the basis functions are illustrated. Notice that the circular current basis function easily can be generalized to cover a circular ring rather than a disc.

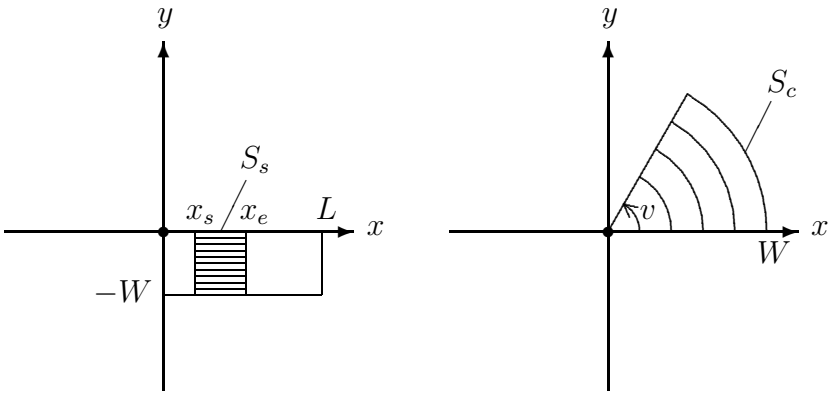

Figure 1: The support of the generic straight section basis functions and the circular current basis function. The dots at the origins are the insertion points.

2.2 Tools for the assembly

By moving, reflecting and rotating the generic basis functions, *i.e.*, the generic straight section basis functions and the circular current basis function, the element is assembled. The translation, reflection and rotation is performed by dyadics in the spatial domain, but may as well be performed in the spectral domain. In fact, it is most efficient to compute the Fourier transform of the generic basis functions and then translate, reflect and rotate the basis functions in the spectral domain.

The basis function $\boldsymbol{j}(\boldsymbol{\rho})$ is simply moved Δx unit lengths in the x-direction and Δy unit lengths in the y-direction by subtracting $\Delta\boldsymbol{\rho} := \hat{x}\Delta x + \hat{y}\Delta y$ from its argument as $\boldsymbol{j}(\boldsymbol{\rho} - \Delta\boldsymbol{\rho})$. The dyadic $\overline{\overline{R}}_\phi := \overline{\overline{I}}_2 \cos\phi + \overline{\overline{J}}_2 \sin\phi$ performs a rotation by an angle ϕ in the right-hand direction around the z-axis. Here, $\overline{\overline{I}}$ is the unit dyadic, while $\overline{\overline{I}}_2 := \hat{x}\hat{x} + \hat{y}\hat{y}$ is the two-dimensional unit dyadic. The dyadic $\overline{\overline{J}}_2$ is defined as $\overline{\overline{J}}_2 := \hat{z} \times \overline{\overline{I}}_2$. We have $\det \overline{\overline{R}}_\phi = 1$, and moreover, $\overline{\overline{R}}_\phi^t = \overline{\overline{R}}_\phi^{-1}$, where $\overline{\overline{R}}_\phi^t$ and $\overline{\overline{R}}_\phi^{-1}$ denote the transpose and inverse of the dyadic $\overline{\overline{R}}_\phi$, respectively. The basis function $\boldsymbol{j}(\boldsymbol{\rho})$ is rotated by an angle ϕ in the right-hand direction around the z-axis as

$$\overline{\overline{R}}_\phi \cdot \boldsymbol{j}(\overline{\overline{R}}_\phi^t \cdot \boldsymbol{\rho}) \tag{2.3}$$

Finally, we introduce the dyadic $\overline{\overline{S}}_u := \overline{\overline{I}} - 2\hat{u}\hat{u}$, which performs a reflection in the $\boldsymbol{r} \cdot \hat{u} = 0$ plane. We have $\det \overline{\overline{S}}_u = -1$, and moreover, $\overline{\overline{S}}_u = \overline{\overline{S}}_u^t = \overline{\overline{S}}_u^{-1}$. The basis function $\boldsymbol{j}(\boldsymbol{\rho})$ is reflected in the $\boldsymbol{r} \cdot \hat{u} = 0$ plane as

$$\overline{\overline{S}}_u \cdot \boldsymbol{j}(\overline{\overline{S}}_u \cdot \boldsymbol{\rho})$$

2.3 Center connected elements

Generally, it is not sufficient that the center connected element is covered by basis functions, since it is also necessary that the basis functions used are able to approximate the induced current in the frequency range considered. This is not all bad

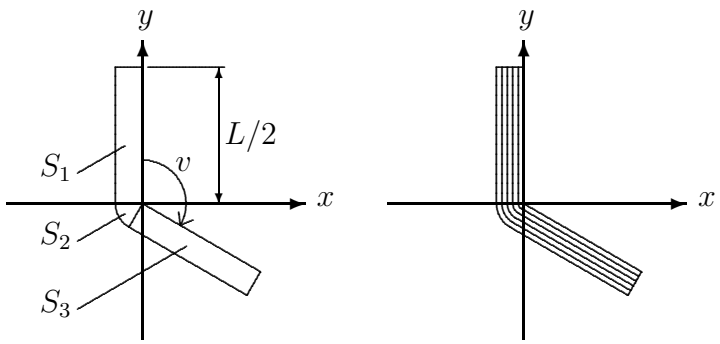

Figure 2: The open sets S_1, S_2 and S_3, and the current lines of the V-dipole basis functions.

since the one who is forced to define the basis function structure will gain physical insight into how the scatterers operate. In this paper we consider the tripole to show how the V-dipole basis functions are adapted to a center connected element. However, the V-dipole basis functions can be adapted to any center connected element, see [8] for a general approach, where the key is to recognize the tree structure of the element.

The tripole considered here is divided into V-dipoles. Each V-dipole consists of two linear arms (straight sections) and a bend (circular current). The *V-dipole basis functions* $\boldsymbol{j}_p^V(\boldsymbol{\rho}; v)$ are defined on the open sets S_n (defined below) as

$$\boldsymbol{j}_p^V(\boldsymbol{\rho}; v) := \begin{cases} \overline{\overline{R}}_{-90^\circ} \cdot \boldsymbol{j}_p^{0-L/2}(\overline{\overline{R}}^t_{-90^\circ} \cdot \boldsymbol{\rho}) & \boldsymbol{\rho} \in S_1 \\ \overline{\overline{R}}_{180^\circ} \cdot \boldsymbol{j}^c(\overline{\overline{R}}^t_{180^\circ} \cdot \boldsymbol{\rho}; v) & \boldsymbol{\rho} \in S_2 \\ \overline{\overline{R}}_{90^\circ - v} \cdot \boldsymbol{j}_p^{L/2-L}(\overline{\overline{R}}^t_{90^\circ - v} \cdot \boldsymbol{\rho}) & \boldsymbol{\rho} \in S_3 \end{cases} \tag{2.4}$$

where $\boldsymbol{j}_p^{0-L/2}(\boldsymbol{\rho}) := \boldsymbol{j}_p^+(\boldsymbol{\rho} + \hat{x}L/2; 0, L/2)$ and $\boldsymbol{j}_p^{L/2-L}(\boldsymbol{\rho}) := \boldsymbol{j}_p^+(\boldsymbol{\rho} + \hat{x}L/2; L/2, L)$, $p \geq 1$. The open sets S_n are illustrated in Figure 2. Specifically, we have

$$S_1 := \{\boldsymbol{\rho} \in \mathbb{R}^2 : -W < x < 0, 0 < y < L/2\}$$
$$S_2 := \{\boldsymbol{\rho} \in \mathbb{R}^2 : 0 < \rho < W, v < \arccos x/\rho < \pi, y < 0\}$$

and

$$S_3 := \{\overline{\overline{R}}_{-v} \cdot \overline{\overline{S}}_x \cdot \boldsymbol{\rho} : \boldsymbol{\rho} \in S_1\}$$

The angle of the V-dipole basis functions is in the interval $0 < v < 180^\circ$. The V-dipole basis functions can be adapted to a specific element geometry by moving and rotating the basis functions in the xy-plane, and of course, by adjusting the angle v.

The V-dipole basis functions, (2.4), can easily be generalized to have more than one bend, which is necessary for more advanced element geometries, *e.g.*, the anchor element. To illustrate the approach, the V-dipole basis functions are now adapted to the tripole geometry given by Figure 3. First we set $v = 120^\circ$. The tripole is divided

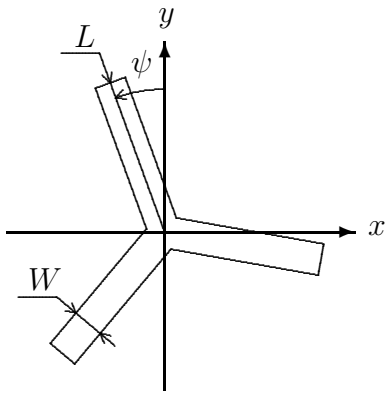

Figure 3: The geometry of the tripole.

into three V-dipoles, where each V-dipole consists of two tripole arms, connected at the center of the tripole. The V-dipole basis functions for the tripole geometry are defined as

$$\begin{cases} \boldsymbol{j}_p^1(\boldsymbol{\rho}) := \boldsymbol{j}_p^V(\boldsymbol{\rho} - \Delta\boldsymbol{\rho}; 120^\circ) \\ \boldsymbol{j}_p^2(\boldsymbol{\rho}) := \overline{\overline{R}}_{120^\circ} \cdot \boldsymbol{j}_p^1(\overline{\overline{R}}_{120^\circ}^t \cdot \boldsymbol{\rho}) \\ \boldsymbol{j}_p^3(\boldsymbol{\rho}) := \overline{\overline{R}}_{-120^\circ} \cdot \boldsymbol{j}_p^1(\overline{\overline{R}}_{-120^\circ}^t \cdot \boldsymbol{\rho}) \end{cases}$$

where $\overline{\overline{R}}_\phi$ is the rotation dyadic defined above, and the shift of origin is defined as $\Delta\boldsymbol{\rho} := W/2(\hat{x}+\hat{y}\tan(\pi/2-v/2))$. The shift of origin is necessary because the tripole element is centered about the origin, while the generic V-dipole basis functions are not. So far one of the tripole arms are parallel to the y-axis, that is, the angle ψ of Figure 3 has not been introduced yet. Hence, as a last step, we rotate the tripole element by an angle ψ in the right-hand direction around the z-axis. Moreover, we use the following enumeration of the basis functions, *i.e.*, the index is mod 3,

$$\boldsymbol{j}_p(\boldsymbol{\rho}) := \begin{cases} \overline{\overline{R}}_\psi \cdot \boldsymbol{j}_{(p+2)/3}^1(\overline{\overline{R}}_\psi^t \cdot \boldsymbol{\rho}) & p = 1, 4, 7, \ldots \\ \overline{\overline{R}}_\psi \cdot \boldsymbol{j}_{(p+1)/3}^2(\overline{\overline{R}}_\psi^t \cdot \boldsymbol{\rho}) & p = 2, 5, \ldots \\ \overline{\overline{R}}_\psi \cdot \boldsymbol{j}_{p/3}^3(\overline{\overline{R}}_\psi^t \cdot \boldsymbol{\rho}) & p = 3, 6, \ldots \end{cases}$$

where the angle of rotation, ψ, is illustrated in Figure 3.

At the arms of the tripole, *i.e.*, at $S_1 \cup S_3$, the basis functions for $p = 1, 2, 3$ are identical with the standard cosine basis functions, *e.g.*, given by Vardaxoglou and Parker [25]. These basis functions approximate the surface current at the first resonance. However, at S_2, the V-dipole basis functions correspond to circular currents of constant amplitude, like the wedge basis functions given by Imbraile, Galindo-Israel, and Rahmat-Samii [9]. The basis functions $\boldsymbol{j}_p(\boldsymbol{\rho})$, for $p = 4, 5$ and 6, are intended to approximate the surface current at the second resonance, and these basis functions are identical with the standard sine basis functions [3, 25]. Higher values of p give repeatedly 3 even (cosine) and 3 odd (sine) basis functions, of higher and higher order.

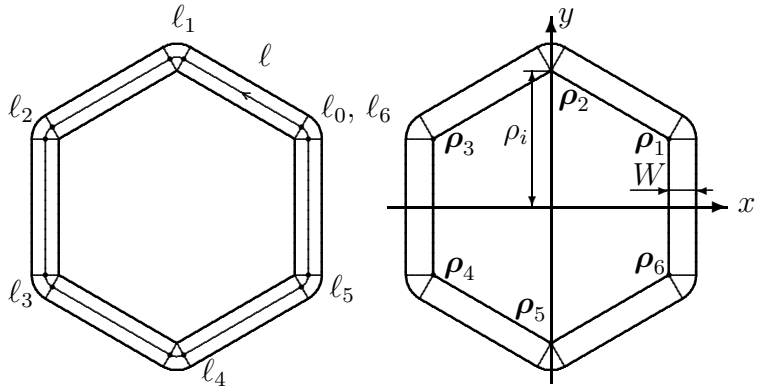

Figure 4: The coordinate ℓ, measuring the distance around the loop, is illustrated to the left, while the insertion points $\boldsymbol{\rho}_n$ are depicted to the right.

2.4 Elements of loop type

In the previous section, the approach for center connected elements was to divide the element into several V-dipoles, and locate one basis function, or several basis functions, on each V-dipole, by moving and rotating the basis function in the xy-plane. However, when analyzing the loop type elements our approach is slightly different. We follow the idea of Au, Musa, Parker and Langley [3], but in this paper the current is bent continuously at the corners, by the circular current basis function (2.2).

In the master's thesis of Åkerberg [1], the V-dipole basis functions were applied to the tripole loop. Without loss of generality, we demonstrate the approach on the hexagonal loop element. The hexagonal element is divided into straight sections and bends according to Figure 4. We introduce a coordinate ℓ along the loop, measuring the distance around the loop from an origin taken at the point ℓ_0 in Figure 4. Hence, ℓ is in the interval $0 \leq \ell \leq L$, where L is the total length of the loop, *e.g.*, the *inner* circumference of the loop. We introduce the coordinates

$$\ell_n := nL/6 = n\rho_i, \quad n = 0, 1, \ldots, 6$$

around the loop. As before, we move and rotate the generic straight section basis functions, (2.1), so that they are adapted to the geometry of the loop. The generic straight section basis function $\boldsymbol{j}_p^\circ(\boldsymbol{\rho}; 0, L)$ is divided into 6 parts as $\boldsymbol{j}_p^\circ(\boldsymbol{\rho}; \ell_{n-1}, \ell_n)$, where $n = 1, 2, \ldots, 6$. Each of these parts are then rotated and moved to their location on the loop. First we define the translated straight section basis functions $\boldsymbol{j}_{p;n}^s(\boldsymbol{\rho})$ as

$$\boldsymbol{j}_{p;n}^s(\boldsymbol{\rho}) := \boldsymbol{j}_p^\circ(\boldsymbol{\rho} + \hat{x}\ell_{n-1}; \ell_{n-1}, \ell_n), \quad n = 1, 2, \ldots, 6$$

These basis functions have support in the region $0 \leq x \leq L/6$, $-W \leq y \leq 0$. The basis functions $\boldsymbol{j}_{p;n}^s(\boldsymbol{\rho})$ are then easily rotated by (2.3). Since the rotation is performed around the z-axis, one corner of the straight section remains at the origin. This corner is called the insertion point. After an appropriate rotation by (2.3), the straight section $\boldsymbol{j}_{p;n}^s(\boldsymbol{\rho})$ is translated in the plane so that the insertion point is located

at the point $\boldsymbol{\rho}_n$, where the points $\boldsymbol{\rho}_n$ are defined as $\boldsymbol{\rho}_n := \hat{x}\rho_i \cos(30^\circ + (n-1)60^\circ) + \hat{y}\rho_i \sin(30^\circ + (n-1)60^\circ)$. Here, ρ_i is the radius of the circle which circumscribes the inner hexagon, see Figure 4. The straight section basis function which is inserted at $\boldsymbol{\rho}_n$ is rotated $\varphi_n := n60^\circ + 90^\circ$ in the right hand direction around the z-axis. To sum up, at the straight sections we apply

$$\boldsymbol{j}_p^s(\boldsymbol{\rho}) := \sum_{n=1}^{6} \overline{\overline{R}}_{\varphi_n} \cdot \boldsymbol{j}_{p;n}^s(\overline{\overline{R}}_{\varphi_n}^t \cdot (\boldsymbol{\rho} - \boldsymbol{\rho}_n)) \tag{2.5}$$

At the bends we apply the circular current basis function (2.2). The circular current basis function at $\boldsymbol{\rho}_n$ is rotated $\phi_n := (n-1)60^\circ$ in the right hand direction around the z-axis. Moreover, to obtain continuity of current from one segment to the next segment, the amplitude of the circular current basis function at $\boldsymbol{\rho}_n$ is $j_p^s(\ell_{n-1}; 0, L)$. This requirement of continuity is necessary, else the double infinite sum of Floquet modes, occurring as matrix elements in the spectral Galerkin method [24], will not converge [19, 26]. If the requirement of continuity is not provided the current along the strip senses a termination of the conductor [9]. To sum up, at the bends we apply

$$\boldsymbol{j}_p^c(\boldsymbol{\rho}) := \sum_{n=1}^{6} j_p^s(\ell_{n-1}; 0, L)\, \overline{\overline{R}}_{\phi_n} \cdot \boldsymbol{j}^c(\overline{\overline{R}}_{\phi_n}^t \cdot (\boldsymbol{\rho} - \boldsymbol{\rho}_n); 60^\circ)$$

Notice that the amplitude is constant at the bends, and that the amplitude and direction of the current at the bends are given by the factor $j_p^s(\ell_{n-1}; 0, L)$, which can be either negative, zero or positive. Hence, for the hexagonal loop we use the V-dipole basis functions

$$\boldsymbol{j}_p(\boldsymbol{\rho}) := \boldsymbol{j}_p^s(\boldsymbol{\rho}) + \boldsymbol{j}_p^c(\boldsymbol{\rho}), \quad p = 0, 1, 2, \ldots \tag{2.6}$$

2.5 The spatial Fourier transform

The Fourier transform operator $\mathcal{F}$ is defined as

$$\mathcal{F}\{\boldsymbol{j}(\boldsymbol{\rho})\}(\boldsymbol{\tau}) := \int_{\mathbb{R}^2} \boldsymbol{j}(\boldsymbol{\rho}) e^{-i\boldsymbol{\rho}\cdot\boldsymbol{\tau}}\, dx\, dy = \tilde{\boldsymbol{j}}(\boldsymbol{\tau})$$

where $\boldsymbol{\tau}$ is the spectral variable. The basis function $\boldsymbol{j}(\boldsymbol{\rho})$ is moved Δx unit lengths in the x-direction and Δy unit lengths in the y-direction by subtracting $\Delta\boldsymbol{\rho} := \hat{x}\Delta x + \hat{y}\Delta y$ from its argument as $\boldsymbol{j}(\boldsymbol{\rho} - \Delta\boldsymbol{\rho})$. The Fourier transform of the translated basis function is easily obtained as

$$\mathcal{F}\{\boldsymbol{j}(\boldsymbol{\rho} - \Delta\boldsymbol{\rho})\}(\boldsymbol{\tau}) = e^{-i\Delta\boldsymbol{\rho}\cdot\boldsymbol{\tau}} \tilde{\boldsymbol{j}}(\boldsymbol{\tau}) \tag{2.7}$$

Moreover, we have also seen that it is convenient to rotate the basis functions. According to (2.3), the basis function $\boldsymbol{j}(\boldsymbol{\rho})$ is rotated by an angle ϕ in the right-hand direction around the z-axis as $\overline{\overline{R}}_\phi \cdot \boldsymbol{j}(\overline{\overline{R}}_\phi^t \cdot \boldsymbol{\rho})$. It is straightforward to show that the Fourier transform of the rotated basis function is given as

$$\mathcal{F}\{\overline{\overline{R}}_\phi \cdot \boldsymbol{j}(\overline{\overline{R}}_\phi^t \cdot \boldsymbol{\rho})\}(\boldsymbol{\tau}) = \overline{\overline{R}}_\phi \cdot \tilde{\boldsymbol{j}}(\overline{\overline{R}}_\phi^t \cdot \boldsymbol{\tau}) \tag{2.8}$$

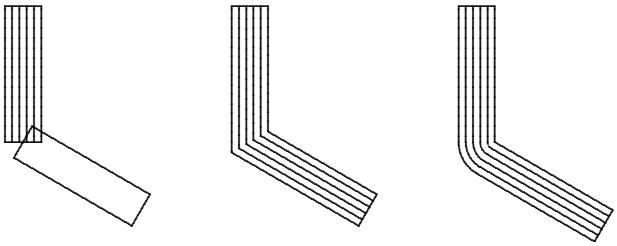

Figure 5: The current lines of the different types of tripole bases intended to approximate the induced surface current density at the first resonance. In all three cases the current is zero at the ends of the tripole arms, and has unit amplitude at the center of the tripole.

Notice that (2.8) is also valid for reflection dyadics as well. The Fourier transform of the generic straight section and the circular current basis functions are given in the appendix.

3 Results

The spectral Galerkin method [24], the presented V-dipole basis functions, and the rotation dyadic $\overline{\overline{R}}_\phi$ were implemented in Fortran 90. The numerical integrations, see the appendix, were performed by the *IMSL Math/Library*, using the adaptive general routine `QDAG`. All computations were made in double precision.

3.1 The tripole array

FSSs comprised of tripoles have been studied extensively in the last two decades [3, 6, 14, 18, 25]. The basis functions used have the standard cosinusoidal and sinusoidal forms, with the requirement that the current should be zero at the ends of the tripole arms. The sine basis functions, introduced to approximate the surface current density at the second resonance, vanish also at the center of the tripole. The cosine basis functions are intended to approximate the current at the first fundamental resonance. The cosine basis function of Vardaxoglou and Parker [25] covers one arm of the tripole, and has unit amplitude at the center. On the other hand, the cosine basis function of Au, Musa, Parker and Langley [3] covers two arms of the tripole (*i.e.*, it covers a V-dipole), and the current changes direction on a line at the center of the tripole, see Figure 5.

Riggs and Smith [21] use a singular expansion method (SEM) on a single tripole to obtain a set of very efficient basis functions. However, the drawback of their method is that they have to recalculate the SEM modes for each set of parameters (the length of the tripole arms *etc.*). Since this recalculation is rather time consuming the SEM is not practical in all applications.

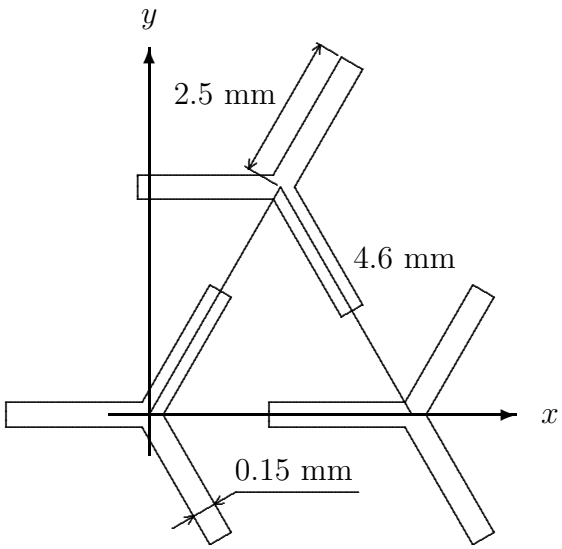

Figure 6: The equilateral triangular lattice. The length and width of the tripole arms are $L = 2.5$ and $W = 0.15$ mm, respectively.

The existing cosine basis functions do not apply to the necessary continuity condition of entire domain basis functions [19], and thus the cosine basis functions are unsuitable with the spectral Galerkin method. Numerically, this shows up when we try to find an appropriate truncation of the double infinite sum of Floquet modes corresponding to a cosine basis function, since this sum is divergent. Therefore, the result is strongly dependent of how many Floquet modes that are included (see Section 3.3).

We consider an FSS comprised of an infinite array of tripoles, where the arms of the tripoles have the lengths $L = 2.5$ mm, and the widths $W = 0.15$ mm. The tripoles are arranged on an equilateral triangular lattice, with the side 4.6 mm, see Figure 6. The angle of rotation is $\psi = -30°$, see Figure 3. Moreover, the tripoles are printed on a substrate, 0.037 mm thick, with $\epsilon = 3$.

This geometry has also been studied by Vardaxoglou and Parker [25], and they have measured the transmission at a number of frequencies at the Ku, K and Ka band (12.4–40 GHz). The transmission is measured for parallel polarization, and the angles of incidence are given by $\theta = 45°$ and $\phi = 90°$, where θ is measured from the normal of the FSS, *i.e.*, the z-axis, such that $\theta = 0°$ corresponds to normal incidence. Furthermore, the angle ϕ is measured from the x-axis towards the y-axis.

We calculate the transmission and compare our computed results with Vardaxoglou and Parker's measured ones. The computations are performed with the spectral Galerkin method [24], and with 2 V-dipole basis functions taken into account, namely $\boldsymbol{j}_1(\boldsymbol{\rho})$ and $\boldsymbol{j}_2(\boldsymbol{\rho})$. Hence, the matrix in the linear system of equations, for the induced surface current, has the size 2×2. The effect of including more basis functions has been investigated, but no significant change of the results was found. However, if a larger frequency band is considered, *e.g.*, a frequency band including

the second resonance, more basis functions have to be included in order to get adequate results. Moreover, 33^2 Floquet modes are included, *i.e.*, the double infinite sums of Floquet modes (occurring as matrix entries) are truncated over a square, *i.e.*,

$$\sum_{m=-\infty}^{\infty}\sum_{n=-\infty}^{\infty} \text{ is truncated as } \sum_{m=-N}^{N}\sum_{n=-N}^{N} \tag{3.1}$$

where $N = 16$. This truncation is determined by adding Floquet modes until the result does not change, see also Figure 11. Notice that the approach is to find out when the matrix elements converge, rather than determining an optimal truncation according to the phenomenon of relative convergence [26]. The substrate is taken into account by a full wave approach [11, 12]. The result is shown in Figure 7. The dashed curve is calculated by the PMM program [15], with 5 PWS current modes (piecewise sinusoidal) taken into account. With 5 modes, PMM predicts also the second resonance, although it is not included in the frequency range considered. Essentially the same result was obtained when including only 2 current modes in PMM (two PWS modes bended at the center of the tripole). From Figure 7 it is concluded that the agreement between the results obtained by the V-dipole basis functions and PMM is extremely good. Figure 7 shows that adequate results can be obtained with a *few good* basis functions. However, generally, more basis functions should be included.

3.2 The hexagonal loop array

As a second example we consider an array of hexagonal loop elements. The inner radius ρ_i and the width W of the loop are illustrated in Figure 4. The radius $\rho_i = 5$ mm, and the width of the loop is $W = 0.866$ mm. The loops are arranged on an equilateral triangular lattice with the side 12 mm, see Figure 6 for a similar lattice.

The angles of incidence are chosen as $\theta = 30^\circ$ and $\phi = 0^\circ$. The incident field is parallel polarized. Moreover, $(2 \times 10 + 1)^2$ Floquet modes and 10 V-dipole basis functions for the hexagonal loop, (2.6), were included. This truncation was achieved so that inclusion of more modes (Floquet and current) will only have a negligeable impact on the result. The result is shown in Figure 8, where the black dots are computed by the hybrid FEM/MoM approach [27]. As depicted in the figure, the FSS is in resonance at approximately 10 GHz. At this frequency the total length of the loop is one wavelength, that is $L = \lambda_0$, where λ_0 is the free space wavelength. The resonance at 10 GHz is the first fundamental resonance of the FSS.

We compare the predicted reflection with the results obtained by a different approach [27], based on a hybrid FEM/MoM formulation for thick screens. The small deviation in the results, showing up as a small shift in frequency (0.1 GHz), can be due to the fact that transversal current is neglected in the V-dipole basis functions, while in the hybrid method, a complete set of modes is used [27]. Moreover, the V-dipole basis functions do not satisfy the edge condition which requires that the current component parallel to an edge is singular. The effect of reducing the width of the loop to $W = 0.433$ mm, while the radius ρ_i is unaltered, has been investigated.

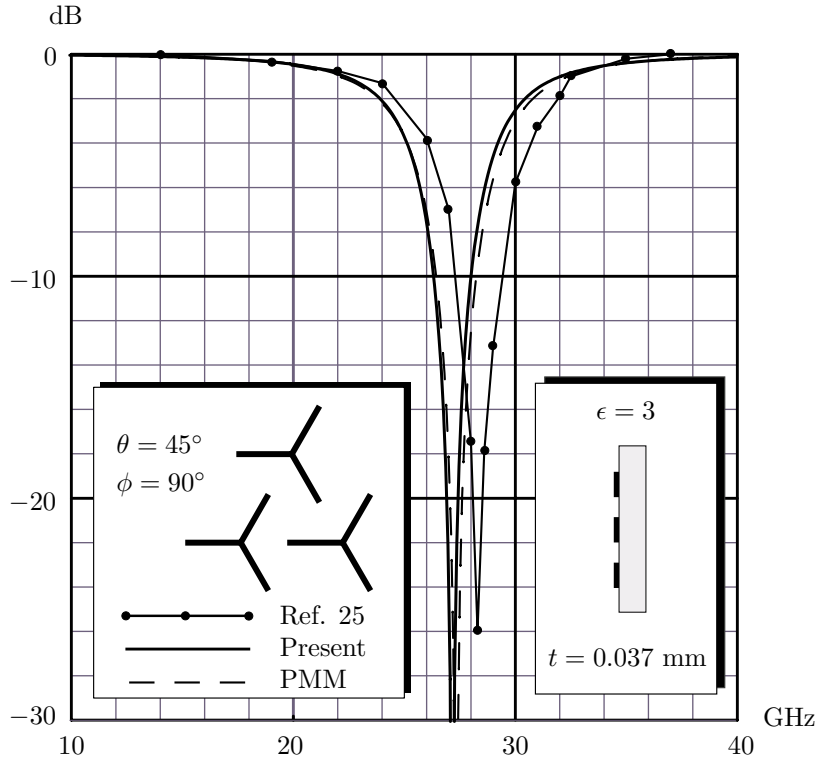

Figure 7: Predicted and measured transmission for parallel polarization. The dots correspond to measured transmission [25], while the dashed curve is computed by the PMM program [15]. The solid curve is computed with 2 V-dipole basis functions. The angle of incidence is $\theta = 45°$.

It was found that the deviation, seen as a frequency shift of 0.1 GHz, still remained.

The dashed curve in Figure 8 is computed by the PMM program [15], with 12 current modes (piecewise sinusoidal). In general, not only for the elements considered here, good agreement is found between results obtained by PMM and the V-dipole basis functions.

3.3 Convergence of the solution

In section 3.1 we noticed that the discontinuous cosine basis functions proposed by other authors [3, 25], see Figure 5, do not apply to the necessary continuity condition of entire domain basis functions [19]. The main drawback of discontinuous bases is that the resonance frequency obtained from the MoM procedure is strongly dependent of how many Floquet modes which are taken into account. The main objective of this section is to illustrate this fact. Therefore, we consider the tripole array of Figure 6. We calculate the reflection coefficient for parallel polarization (see Figure 7 where the transmission coefficient is depicted) using the present V-dipole basis functions and existing bases [3, 25], see Figure 5. In all cases, three basis functions are used. We include more and more Floquet modes and examine

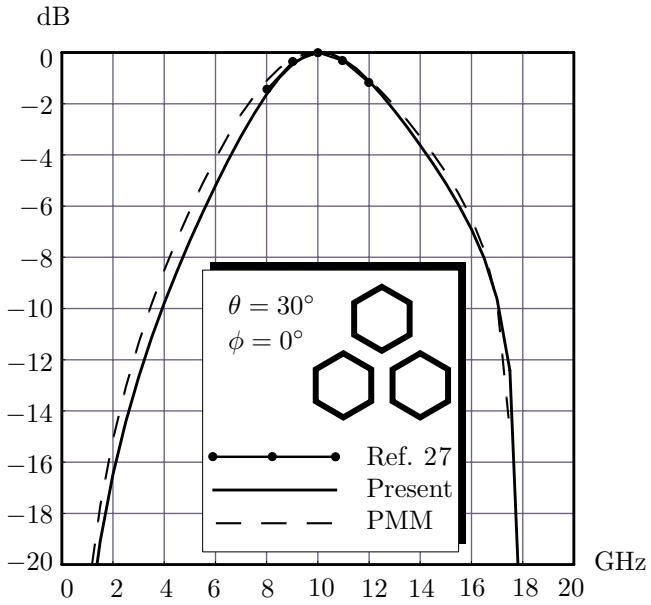

Figure 8: Predicted reflection of hexagonal loop array for parallel polarization. The dotted curve corresponds to reflection coefficients computed by a hybrid MoM/FEM method [27], while the dashed curve is computed by PMM [15]. The solid curve is computed by 10 V-dipole basis functions. The angle of incidence is 30°.

how the result converges. Firstly, we examine the convergence for a free standing FSS without substrate. In Figure 9 the resonance frequency of the tripole array is plotted as a function of the number of Floquet modes included, *i.e.*, as a function of N, see (3.1). It is concluded that convergence is obtained when the present V-dipole basis functions are used, since the resonance frequency does not change for $N \geq 6$. Generally, when continuous bases are used, we simply include Floquet modes until the result does not change [19], which means that in this case we chose $N \geq 6$. On the other hand, when discontinuous bases are used, we are forced to include an optimal number of Floquet modes, that is, not too many and not too few Floquet modes. For instance, when using the cosine base of [3], from Figure 9 it is concluded that it is necessary to include about $(2N+1)^2$ Floquet modes, where $N = 13$, otherwise the obtained results will not be adequate. This means that when discontinuous bases are used, we need a rule of thumb in order to adequately establish the truncation parameter N.

We now investigate the convergence when the FSS is supported by a substrate. In Figure 10 the substrate is taken into account by the scattering matrix approach [4]. We include Floquet waves (plane waves) up to order 4, *i.e.*, the size of the scattering matrices is 162×162. Again, absolute convergence is found for the present base. In fact, the convergence results are similar to the ones obtained for the free standing FSS. This is not surprising, since in the scattering matrix approach, we first calculate the scattering matrices for the free standing FSS and substrate, respectively, and then the scattering matrix of the cascaded structure is obtained by simple matrix

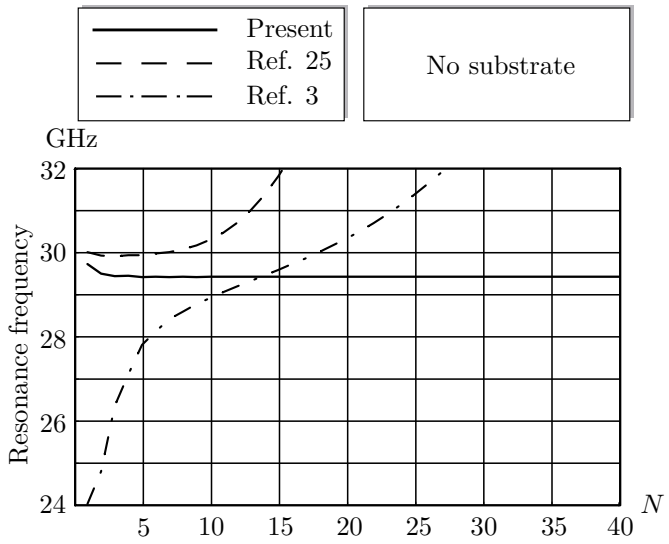

Figure 9: The resonance frequency vs. the number of Floquet modes included for the tripole array of Figure 6, but without the dielectric substrate. The angles of incidence are $\theta = 45°$ and $\phi = 90°$.

algebra. However, when using the full wave method [11, 12], the current distribution found by the method of moments is calculated with the substrate present. Hence, the convergence of the double infinite Floquet sums is affected by the actual substrate. In Figure 11 the convergence is shown when the full wave method is used. Convergence is found for the present base, and the resonance frequency converges to $f_1 = 27$ GHz as the number of Floquet modes approaches infinity. Hence, the resonance frequency is reduced 8.5% when the substrate is introduced, see Figure 9. When using the scattering matrix approach, see Figure 10, the resonance frequency was reduced 3% only. It is found that the discrepancy, 8.5% compared to 3% reduction, is reduced when more Floquet waves (plane waves) are included. However, that would require larger scattering matrices, and due to computer limitations, we have not been able to investigate the effect of including more Floquet waves. The size of the scattering matrices is $2(2M + 1)^2 \times 2(2M + 1)^2$, where M is the index of the highest order Floquet wave included. This poor convergence of the scattering matrix approach can be avoided by letting a part of the substrate support the FSS, such that the evanescent waves radiated from the FSS are suppressed in the supporting substrate [22].

Numerous methods have been used to analyze FSSs. It is important to notice that the convergence results given here is valid for the spectral Galerkin method [24], and that they are not necessarily true for other methods, for instance the equivalent circuit method.

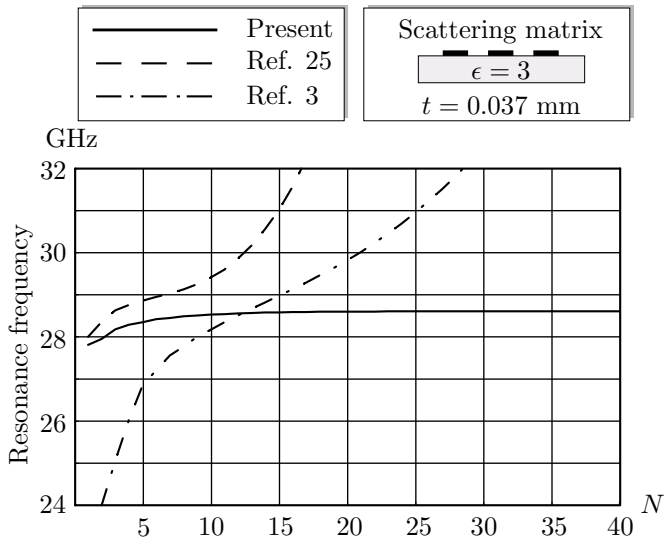

Figure 10: Same case as in Figure 9, but here the FSS is supported by a dielectric substrate. The effect of the substrate is computed by the scattering matrix approach [4].

4 Conclusions

In this paper an efficient set of V-dipole basis functions was introduced. Their application to center connected and loop type elements was demonstrated. The elements of these two groups are the far most interesting when it comes to practical applications. Combinations, *e.g.*, a tripole inside a hexagonal loop, can be treated as well. The element was divided into straight sections and bends, and by simple translation and rotation, the so called generic straight section basis functions and the circular current basis function were positioned to cover the element. The translation and rotation can be performed either in the spatial domain or in the spectral domain.

First we considered the tripole element, which was divided into three V-dipoles. Excellent agreement between predicted and measured transmission was found, even when only 2 of the present V-dipole basis functions were taken into account. Regarding the hexagonal loop element, we compared our predicted results with results obtained by PMM [15] and a hybrid FEM/MoM approach [27].

The present basis functions do not satisfy the edge condition which requires that the current component parallel to an edge is singular. One reason for why this edge condition was not introduced is that in the case of center connected elements, the singular edge would occur at the interior of the element, *i.e.*, at the edge of the circular current basis function, since the non-straight boundary of the set S_2 is not located at an edge of the element, see Figure 2. However, for loop type elements, the edge condition does not cause such problems, and it is expected that basis functions with correct edge behavior improve the convergence [2].

Finally, we noticed that absolute convergence of the method of moment solution was obtained when continuous bases are used. However, when discontinuous bases

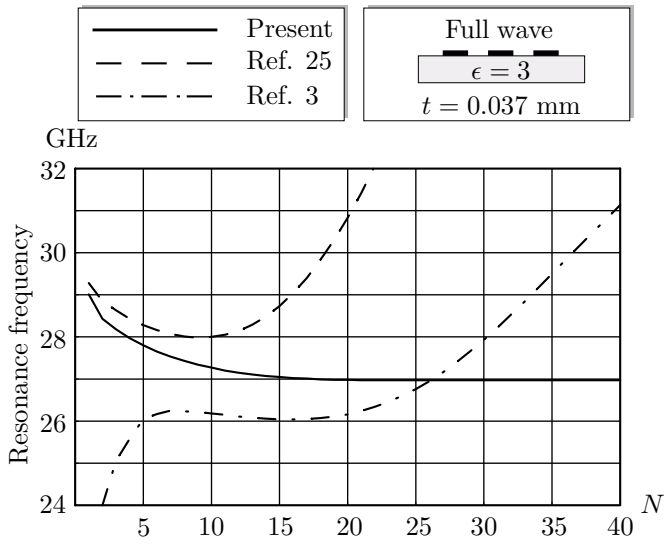

Figure 11: Same case as in Figure 10, but here the effect of the substrate is computed by the full wave approach [11].

are used, the method of moment solution does not converge as the number of Floquet modes are increased. In fact, we found that the double infinite Floquet sum diverges when discontinuous bases are used. Therefore, care needs to be exercised and it would seem discontinuous bases should be avoided.

Appendix A The Fourier transform

The Fourier transform of the circular current basis function is given by

$$\tilde{\boldsymbol{j}}^c(\boldsymbol{\tau}; v) := \int_{S_c} \frac{-\hat{x}y + \hat{y}x}{\sqrt{x^2+y^2}} e^{-i\boldsymbol{\rho}\cdot\boldsymbol{\tau}}\, dx\, dy$$

In polar coordinates ρ and ϕ, this integral can be written

$$\tilde{\boldsymbol{j}}^c(\boldsymbol{\tau}; v) = \int_0^W \rho\, d\rho \int_0^v d\phi \left\{-\hat{x}\sin\phi + \hat{y}\cos\phi\right\} e^{-i\rho\tau\cos(\phi-\varphi)}$$

where $\boldsymbol{\tau} = \hat{x}\tau\cos\varphi + \hat{y}\tau\sin\varphi$. We substitute $\xi = \phi - \varphi$ and notice that

$$\begin{cases} \sin(\xi+\varphi) = \sin\xi\cos\varphi + \cos\xi\sin\varphi \\ \cos(\xi+\varphi) = \cos\xi\cos\varphi - \sin\xi\sin\varphi \end{cases}$$

The result is

$$\begin{aligned} \tilde{\boldsymbol{j}}^c(\boldsymbol{\tau}; v) &= \int_0^W \rho\, d\rho \int_{\varphi-v}^{\varphi} d\xi \left\{\hat{x}(\sin\xi\cos\varphi - \cos\xi\sin\varphi)\right. \\ &\quad \left. + \hat{y}(\cos\xi\cos\varphi + \sin\xi\sin\varphi)\right\} e^{-i\rho\tau\cos\xi} \\ &= \int_0^W \rho\, d\rho \int_{\varphi-v}^{\varphi} d\xi \left\{\hat{\tau}\sin\xi + \hat{\varphi}\cos\xi\right\} e^{-i\rho\tau\cos\xi} \end{aligned}$$

where $\hat{\tau} := \hat{x}\cos\varphi + \hat{y}\sin\varphi$ and $\hat{\varphi} := -\hat{x}\sin\varphi + \hat{y}\cos\varphi$. Two integrals can be identified, $\tilde{j}^c_\tau(\boldsymbol{\tau}; v)$ and $\tilde{j}^c_\varphi(\boldsymbol{\tau}; v)$, such that

$$\tilde{\boldsymbol{j}}^c(\boldsymbol{\tau}; v) = \hat{\tau}\tilde{j}^c_\tau(\boldsymbol{\tau}; v) + \hat{\varphi}\tilde{j}^c_\varphi(\boldsymbol{\tau}; v)$$

The integral $\tilde{j}^c_\tau(\boldsymbol{\tau}; v)$ can be performed in closed form,

$$\begin{aligned}\tilde{j}^c_\tau(\boldsymbol{\tau}; v) &:= \int_0^W \rho\, d\rho \int_{\varphi-v}^{\varphi} d\xi\, \sin\xi\, e^{-i\rho\tau\cos\xi} \\ &= \Gamma_2(\varphi) - \Gamma_2(\varphi - v)\end{aligned}$$

where $\Gamma_2(\xi) := (e^{-iW\tau\cos\xi} - 1)/\tau^2\cos\xi$. The integral $\tilde{j}^c_\varphi(\boldsymbol{\tau}; v)$ is defined as

$$\tilde{j}^c_\varphi(\boldsymbol{\tau}; v) := \int_0^W \rho\, d\rho \int_{\varphi-v}^{\varphi} d\xi\, \cos\xi\, e^{-i\rho\tau\cos\xi}$$

We perform the integration over ρ and get

$$\tilde{j}^c_\varphi(\boldsymbol{\tau}; v) = \frac{1}{\tau^2}\int_{\varphi-v}^{\varphi}\left(iW\tau e^{-iW\tau\cos\xi} + \frac{e^{-iW\tau\cos\xi} - 1}{\cos\xi}\right) d\xi$$

This integral is performed by numerical integration. Notice that the Fourier transform of the basis functions can be computed and stored once in the beginning of the computation. Finally, the Fourier transform of the generic straight section basis functions $\boldsymbol{j}_p^{+,\circ}(\boldsymbol{\rho}; x_s, x_e)$, see (2.1), is easily expressed in closed form.

Appendix Acknowledgments

I am deeply grateful to my supervisor prof. Gerhard Kristensson, and would like to thank him for his excellent guidance throughout this work. I would also like to thank Björn Widenberg for providing the hybrid FEM/MoM results which we use here for comparison. Furthermore, I am deeply grateful to prof. Ben Munk for the invitation to work in his group at the *ElectroScience Laboratory*, Ohio State University. The work reported in this paper is supported by a grant from the Defence Materiel Administration of Sweden (FMV) and its support is gratefully acknowledged.

References

[1] M. Åkerberg. Scattering from frequency selective surfaces: A set of basis functions for the tripole loop. Master's thesis, Lund Institute of Technology, Department of Electroscience, P.O. Box 118, SE-211 00 Lund, Sweden, 1999. Tech. Rep. LUTEDX/(TEAT-5032)/1–34/(1999).

[2] T. Andersson. Moment-method calculations on apertures using basis singular functions. *IEEE Trans. Antennas Propagat.*, **41**(12), 1709–1716, 1993.

[3] P. W. B. Au et al. Parametric study of tripole and tripole loop arrays as frequency selective surfaces. *IEE Proc.-H Microwaves, Antennas and Propagation*, **137**(5), 263–268, 1990.

[4] T. A. Cwik and R. Mittra. The cascade connection of planar periodic surfaces and lossy dielectric layers to form an arbitrary periodic screen. *IEEE Trans. Antennas Propagat.*, **35**(12), 1397–1405, December 1987.

[5] T. A. Cwik and R. Mittra. Correction to "The cascade connection of planar periodic surfaces and lossy dielectric layers to form an arbitrary periodic screen". *IEEE Trans. Antennas Propagat.*, **36**(9), 1335, September 1988.

[6] J. G. Gallagher and D. J. Brammer. High order resonances and scattering from FSS tripole arrays. In *Proc. 6th Int. Conf. on Antennas and Propagation, IEE Conf. Publ.*, pages 521–525, 1989.

[7] R. C. Hall, R. Mittra, and K. M. Mitzner. Analysis of multilayered periodic structures using generalized scattering matrix-theory. *IEEE Trans. Antennas Propagat.*, **36**(4), 511–518, 1988.

[8] L. W. Henderson. Introduction to PMM, version 4.0. Technical Report 725347-1, ElectroScience Laboratory, Ohio State University, Department of Electrical Engineering, 1320 Kinnear Road, Columbus, Ohio 43212, USA, 1993.

[9] W. A. Imbraile, V. Galindo-Israel, and Y. Rahmat-Samii. On the reflectivity of complex mesh surfaces. *IEEE Trans. Antennas Propagat.*, **39**, 1352–1365, September 1991.

[10] F. S. Johansson. Convergence phenomenon in the solution of dichroic scattering problems by Galerkin's method. *IEE Proc.-H Microwaves, Antennas and Propagation*, **134**, 87–92, February 1987.

[11] G. Kristensson, M. Åkerberg, and S. Poulsen. Scattering from a frequency selective surface supported by a bianisotropic substrate. In J. A. Kong, editor, *Electromagnetic Waves PIER 35*, pages 83–114. EMW Publishing, Cambridge, Massachusetts, 2001.

[12] G. Kristensson, S. Poulsen, and S. Rikte. Propagators and scattering of electromagnetic waves in planar bianisotropic slabs — an application to frequency selective structures. Technical Report LUTEDX/(TEAT-7099)/1–32/(2001), Lund Institute of Technology, Department of Electroscience, P.O. Box 118, S-211 00 Lund, Sweden, 2001.

[13] R. Mittra. Relative convergence of the solution of a doubly infinite set of equations. *J. Nat. Bur. Stand.*, **67D**, 245–254, Mar.–Apr. 1963.

[14] M. M. Mokhtar and E. A. Parker. Conjugate-gradient computation of the current distribution on a tripole FSS array element. *Electronics Letters*, **26**(4), 227–228, 1990.

[15] B. Munk. *Frequency Selective Surfaces: Theory and Design.* John Wiley & Sons, New York, 2000.

[16] B. A. Munk and G. A. Burrell. Plane-wave expansion for arrays of arbitrarily oriented piecewise linear elements and its application in determining the impedance of a single linear antenna in a lossy half-space. *IEEE Trans. Antennas Propagat.*, **27**(3), 331–343, 1979.

[17] B. A. Munk, G. A. Burrell, and T. W. Kornbau. A general theory of periodic surfaces in stratified media. Technical Report 784346-1, ElectroScience Laboratory, Ohio State University, Department of Electrical Engineering, 1320 Kinnear Road, Columbus, Ohio 43212, USA, 1977. Prepared under contract AFAL-TR-77-219.

[18] L. Musa et al. Sensitivity of tripole and calthrop FSS reflection bands to angle of incidence. *Electronics Letters*, **25**(4), 284–285, 1989.

[19] S. Poulsen. Scattering from frequency selective surfaces: A continuity condition for entire domain basis functions and an improved set of basis functions for crossed dipole. *IEE Proc.-H Microwaves, Antennas and Propagation*, **146**(3), 234–240, 1999.

[20] S. Poulsen. *Scattering of electromagnetic waves from frequency selective surfaces.* Licentiate thesis, Lund Institute of Technology, Department of Applied Electronics, Electromagnetic Theory, P.O. Box 118, S-211 00 Lund, Sweden, 2000.

[21] L. S. Riggs and R. G. Smith. Efficient current expansion modes for the triarm frequency-selective surface. *IEEE Trans. Antennas Propagat.*, **36**(8), 1172–1177, 1988.

[22] N. V. Shuley. Higher-order mode interaction in planar periodic structures. *IEE Proceedings*, **131**(3), 129–132, June 1984.

[23] N. V. Shuley. A note on relative convergence for moment-method solutions of integral equations of the first kind as applied to dichroic problems. *Electronics Letters*, **21**(3), 95–97, 1985.

[24] C.-H. Tsao and R. Mittra. Spectral-domain analysis of frequency selective surfaces comprised of periodic arrays of cross dipoles and Jerusalem crosses. *IEEE Trans. Antennas Propagat.*, **32**(5), 478–486, 1984.

[25] J. C. Vardaxoglou and E. A. Parker. Performance of two tripole arrays as frequency-selective surfaces. *Electronics Letters*, **19**(18), 709–710, 1983.

[26] K. J. Webb, P. W. Grounds, and R. Mittra. Convergence in the spectral domain formulation of waveguide and scattering problems. *IEEE Trans. Antennas Propagat.*, **38**, 869–877, June 1990.

[27] B. Widenberg, S. Poulsen, and A. Karlsson. Scattering from thick frequency selective screens. *J. Electro. Waves Applic.*, **14**, 1303–1328, 2000.

[28] T. K. Wu, editor. *Frequency Selective Surface and Grid Array.* John Wiley & Sons, New York, 1995.